Low-loss and wideband acoustic delay lines

Manzaneque Garcia, Tomas; Lu, Ruochen; Yang, Yansong; Gong, Songbin

Important note
To cite this publication, please use the final published version (if applicable).
Please check the document version above.

Low-Loss and Wide-Band Acoustic Delay Lines

Tomás Manzaneque, *Member, IEEE*, Ruochen Lu, *Student Member, IEEE*, Yansong Yang, *Student Member, IEEE*, and Songbin Gong, *Senior Member, IEEE*

Abstract—**This paper demonstrates low-loss acoustic delay lines based on shear-horizontal waves in thin-film LiNbO₃ for the first time. Due to its high electromechanical coupling, the shear-horizontal mode is suited for producing devices with large bandwidths. Here we show that shear-horizontal waves in LiNbO₃ thin films are also excellent for implementing low-loss acoustic delay lines based on unidirectional transducers. The high acoustic reflections and large transducer uni-directionality induced by the mechanical loading of the electrodes on a LiNbO₃ thin film provide a great trade-off between delay line insertion loss and bandwidth. The directionality for two different types of uni-directional transducers has been characterized. Delay lines with variations in the key design parameters have been designed, fabricated and measured. One of our fabricated devices has shown a group delay of 75 ns with an IL below 2 dB over a 3 dB bandwidth of 16 MHz centered at 160 MHz (FBW=10%). The measured insertion loss for other devices with longer delays and different numbers of transducer cells are analyzed, and the loss contributing factors and their possible mitigation are discussed.**

Index Terms— **Acoustic devices, delay lines, lithium niobate, microelectromechanical systems, piezoelectric transducers, transversal filters.**

I. INTRODUCTION

RECENTLY, the expansion of wireless inter-connectivity among autonomous sensors or mobile devices is demanding analog signal processing functions with low loss, small form factors, and low or zero power consumption at radio frequencies (RF) [1]. In this context, acoustic devices constitute an excellent chip-scale and low-loss platform, in which electromagnetic (EM) waves are converted into the acoustic domain for processing, and are subsequently converted back to the EM domain for interfacing with the rest of the system. At RF, the propagation of acoustic waves in the state-of-the-art (SOA) piezoelectric thin films exhibits much lower loss than the propagation of EM waves in planar wave-guiding structures (e.g., Microstrip). Moreover, given the low phase velocities, typically below 10000 m/s, and the low propagation loss of acoustic waves, high-performance wave-guiding structures can be designed with sizes comparable to the acoustic wavelengths, in the 10s of μm range at RF. As a result of the abovementioned benefits in the acoustic domain, wave phenomena can be exploited for signal processing functions (e.g., time delay or transversal filtering) in a very small form factor that otherwise would be inaccessible in the EM domain at RF.

In the past, the study of signal processing functions in the acoustic domain was mainly motivated by enabling radar systems. Surface acoustic wave-guiding structures, namely acoustic delay lines (ADL), were built on piezoelectric bulk substrates, with which the electromechanical transduction from the electrical to the acoustic domain is provided by the piezoelectricity of the material. By storing a received pulse in an ADL for comparison with the next pulse, the scattering from static objects can be canceled, thus diminishing the clutter in radar displays [2], [3]. Following the advances made for radars, other applications for ADLs, such as frequency discriminators [4], [5] and modulators/demodulators for frequency shift keying (FSK) [6], also emerged. These applications all leverage the large time-delay product accessible only in ADLs to introduce delays over a given bandwidth for signal processing. For instance, the FSK-based spread spectrum communication scheme in [6] represents each data symbol with a code formed by a sequence of frequencies at RF. An ADL is then used to impose delays to the incoming signal as a function of its frequency to perform matched filtering before the demodulation of the signal. Naturally, such a function of ADLs can also be dual-purposed as part of a modulator on the transmitter side [7]–[9].

In addition to the various flavors of matched filtering above, perhaps the most pervasive application of ADLs was transversal filtering. Transversal filters based on ADLs offer great flexibility in designing both the amplitude and phase responses while achieving high out-of-band rejection [10]. The operating principle of transversal filtering relies on tapping a delay line at different points [11]. By connecting these taps situated at different sections of the ADL, the output signals are combined in the electrical domain to form a finite Fourier series [12], [13]. With properly designed electrode pitch, polarity, and electrode sections in the ADL, the frequencies, phases, and relative amplitudes of the terms in the Fourier series can be varied to obtain a quasi-arbitrarily configurable filter response. Because of such addressability in their response, transversal filters understandably have been favored over filters based on coupled resonators, such as those based on surface acoustic waves (SAW) [14], lamb waves [15], or thickness modes [16], for certain applications.

More recently, ADLs have found new applications in enabling compact and low-power non-reciprocal networks using time-varying circuit structures [17]–[20]. In these approaches, a pair or an array of acoustic delay lines are controlled and accessed by switches on both ends so that signals are routed between ports on opposite sides of delay lines only in certain allowed paths. Such an approach to engineer chip-scale non-reciprocal response without resorting to magnetic materials is paving new paths for implementing front-ends with the simultaneous transmit and receive capability.

Despite their numerous applications in the past and newly found opportunities, ADLs have seen stagnant progress in performance in the past decade. The lack of advancement is partially due to that signal processing previously implemented by ADLs has been increasingly replaced by digital signal processors (DSP). DSPs can implement complex functions that are programmed in the digital domain with a high degree of flexibility. Typically, the advantages of being capable and easily adaptable justify the need for analog-to-digital conversion (ADC) and computing in DSPs in applications with power budgets in the range of mW [21]. However, the emergence of the internet of things (IoT) is creating new application scenarios where power, cost, and complexity added by ADC and digital computing cannot be afforded. Consequently, ADL-enabled RF signal processing that requires zero power budget is becoming of high interest and relevance again. Although not as programmable or versatile as DSP, ADLs are sufficient for many IoT devices where device-end signal processing needs not to be computationally intense, and meeting the low power budget is a higher priority. Moreover, ADLs are competitive against DSPs in size due to the small wavelengths of acoustic waves at RF, consequently making them suitable for miniature, wearable, or mobile nodes of IoT. In certain scenarios, ADLs can also be seamlessly integrated with several sensing modalities [22], thus making them a holistic solution for wireless sensor nodes in IoT. Nevertheless, to be a truly viable option for IoT, the ADLs have to overcome several bottlenecks that have conventionally limited them from achieving low IL and broad fractional bandwidth (FBW).

The limits on IL and FBW of ADLs are correlated and multifold. ADLs employing interdigital transducers of the simplest type suffer from bi-directionality losses and have a minimum IL of 6 dB [12]. Thus, low-loss ADLs typically adopt unidirectional transducers (UDT) to mitigate such type of loss [23]. Multi-phase transducers [24], [25], or single-phase unidirectional transducers (SPUDT) have been demonstrated [26]–[32]. These designs have embedded distributed acoustic reflectors formed by grounded or floating electrodes in an asymmetrical arrangement with respect to the signal electrodes. The IL of SPUDT-based ADLs depends on the uni-directionality achieved collectively through the reflectors. Therefore, low IL can be attained using either high reflectivity per wavelength or a large number of reflectors, although the latter method comes with reduced FBW. ADLs reported so far are mainly based on surface acoustic waves excited on a piezoelectric substrate made of lithium niobate (LiNbO$_3$), lithium tantalate (LiTaO$_3$),

or quartz. The low electromechanical coupling (k_t^2) values restrict the FBW of bi-directional transducers and limits the reflectivity attained via grounded electrodes. In addition, reflections induced by mechanical loading in SAW structures are quite moderate as the reflector electrodes are relatively insignificant in mass in comparison to the surface portion of the substrate in which surface acoustic waves travel.

To overcome these performance limitations, we resort to LiNbO$_3$ laterally vibrating devices based on plate modes, such as lamb and shear-horizontal waves. They have emerged recently [33] with high electromechanical coupling (k_t^2) and demonstrated FBWs outperforming those of their SAW counterparts [34]. The advantage of the high k_t^2 has already been validated in the broad-band dispersive delay lines [35]. More importantly, the thin-film-based ADLs are more susceptible to mechanical loading, thus producing higher reflectivity per electrode than SAW and a much better design trade between IL and FBW.

In this work, we study and demonstrate ADLs with low loss and large fractional bandwidth based on first-order shear-horizontal waves (SH0) in LiNbO$_3$ thin films. Delay lines with variations in the key design parameters have been designed, fabricated and measured. One of our fabricated devices has shown a delay of 75 ns with an IL below 2 dB over a 3 dB bandwidth of 16 MHz centered at 160 MHz. The measured insertion loss for other devices with longer delays and different numbers of transducer cells are analyzed to extract the loss. The contributing factors and their possible mitigation are discussed.

II. DEVICE DESIGN APPROACH AND ANALYSIS

A. Overview of Delay Line Design

A schematic top view of the delay lines in this paper is presented in Fig. 1(a). A suspended thin film of LiNbO$_3$ constitutes the propagation medium for the SH0 acoustic waves. The thickness of the LiNbO$_3$ thin film has been chosen to be 800 nm due to our fabrication limitation in etching LiNbO$_3$. The analyses onward all use such thickness. Two sets of interdigital transducers (IDT) consisting of metal electrodes interconnected by bus lines are implemented on top of the LiNbO$_3$ thin film. Either set of IDTs can serve as the transmitting transducer (input port), while the other IDT serves as the receiving transducer (output port). The IDTs are separated by a distance L_G that primarily sets the time delay experienced by an electrical signal traversing from the input port to the output port. Each transducer is formed by cascading N identical unit cells, each of which contains two types of electrodes: ground electrodes (green) that are connected to the lower bus line, and signal electrodes (blue) that are connected to the upper bus line in Fig. 1(a). When a voltage is applied between the bus lines, electrical fields are generated between the signal and ground electrodes along the propagation direction (x-axis). Through the inverse piezoelectric effect, the E-fields subsequently launch shear strain and stress waves (SH0) in the xy-plane towards both the +x and –x directions. By reciprocity, the shear stress/strain in the xy-plane associated to an acoustic wave propagating through the receiving IDT generates a voltage difference across
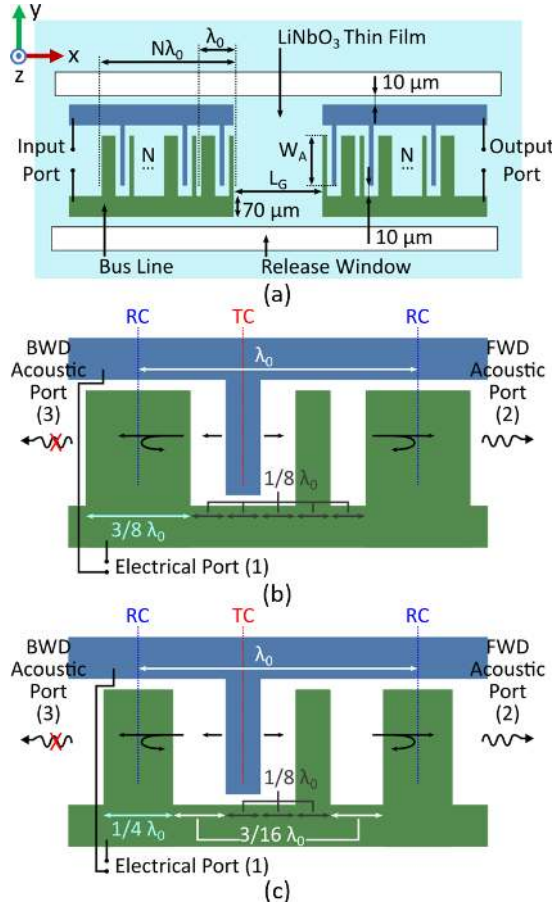
Fig. 1. (a) Top-view of an ADL mock-up consisting of SPUDTs on top of a suspended LiNbO$_3$ thin film. Layouts of (b) DART and (c) EWC unit cells with marked transduction centers (TC) and reflection centers (RC).

the corresponding electrical port. The conversion efficiency between the electrical and acoustic energy is maximum at the center frequency, f_0. At this frequency, the acoustic wave is also phase-delayed by 360⁰ after travelling across a unit cell. The value of f_0 is determined by the length of the unit cells λ_0 as

$$f_0 = \frac{v_t}{\lambda_0}, \qquad (1)$$

where v_t is the average phase velocity of the acoustic wave in the transducer. v_t can be found as the weighted average between the phase velocity of the un-metallized LiNbO$_3$ film v_∞ and the phase velocity of the metallized film v_m, as

$$v_t = \eta\, v_m + (1 - \eta)\, v_\infty, \qquad (2)$$

where η is the metallization ratio of the unit cell. The dependence of f_0 on the film thickness can be neglected, due to the weak dispersive nature of SH0 waves [36].

While the delay line itself can be treated as an electrical device of two ports, the individual transducer, as well as each comprising unit cell, can be analyzed as a three-port network that has one electrical port and two acoustic ports. The two acoustic ports effectively represent the two propagation directions into the acoustic medium. With no directionality, a conventional transducer, also known as a bi-directional transducer, emits the same amount of power towards both acoustic ports. Thus, in a delay line formed by bi-directional transducers and

an acoustic media, only half of the acoustic power available at the input transducer is sent towards the output transducer, while the other half gets lost to the substrate. By reciprocity, the bi-directional output transducer can only convert half of the incident acoustic power to the electric domain. Consequently, ADLs formed by conventional bidirectional transducers suffer from an intrinsic minimum IL of 6 dB.

In order to mitigate the loss due to bi-directionality, single phased unidirectional transducers can be employed. The operation principle of SPUDTs can be explained from the analysis of the transduction and reflection centers founded in their electrode layouts. A transduction center (TC) is defined as a reference plane at which the acoustic waves launched towards both directions have the same amplitude and phase. Similarly, a reflection center (RC) is a reference plane at which the wave reflections from both directions are equal. In conventional IDTs, these centers are evenly and symetrically distributed along the transducer. In SPUDTs, TCs are arranged asymmetrically with respect to the RCs, in a way such that the waves launched, through both transduction and reflection, interfere constructively towards one of the acoustic ports and destructively towards the opposite acoustic port. The former port will be referred to as forward (FWD) and the latter one as backward (BWD) onward. Typically, the TCs are placed closer to the nearest RC on the BWD side than to the nearest RC on the FWD side. The difference between the distances that a TC is from its adjacent RCs must be of $\lambda_0/4$ to produce the mentioned constructive (destructive) interference towards the FWD (BWD) port.

B. Design and Analysis of Unidirectional Transducers

Two types of SPUDTs, known as distributed acoustic reflection transducers (DART) [37] and electrode width controlled (EWC) [38], are explored in this paper. Their unit cells are shown in Fig. 1(b) and (c) respectively. Both designs contain transduction electrodes of width $\lambda_0/8$ and wider electrodes as reflectors. The difference between their unit cells lies in the width of the reflectors. A DART cell employs a reflector electrode of width $3\lambda_0/8$ while an EWC cell uses $\lambda_0/4$.

To locate the TC in the unit cells of Fig. 1(b) and (c), it must first be noted that the shear-horizontal waves are generated through piezoelectricity in the areas with x-polarized electric fields. These areas are the gaps between the signal electrode and the adjacent ground electrodes on both sides. In adjacent gap areas, the x-polarized electric fields induced by the electrodes have opposite signs, as seen in Fig. 2(a). Therefore, in a DART unit cell, the center of the signal electrode is approximately the axis of anti-symmetry for the generated xy-plane strain ϵ_{xy}. Since ϵ_{xy} is the derivative of the y-axis displacement u_y with respect to x, u_y is symmetric with respect to the center of the
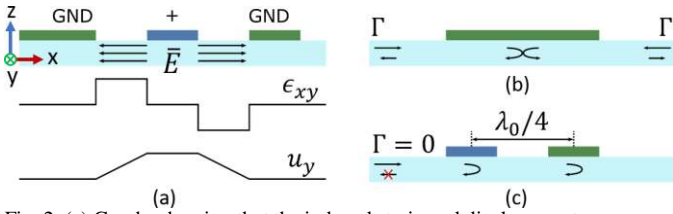
Fig. 2. (a) Graphs showing that the induced strain and displacement are respectively antisymmetric and symmetric with respect to the center of the signal electrode. (b) Equal reflection coefficients referred to the center of the electrode for incidences from both sides. (c) Reflectionless nature of two identical electrodes separated by a distance of $\lambda_0/4$ at f_0.
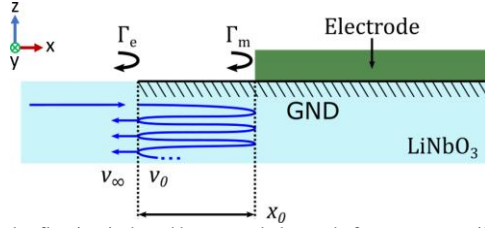

Fig. 3. Total reflection induced by a metal electrode from two contributing components: the electrical and mechanical.

signal electrode. Thus, this point can be considered a TC for the displacement wave $u_y(x,t)$. The same approximation can be adopted for EWC unit cells.

Following the same symmetry rationale for the TC, the center of a reflection electrode can be regarded as a reflection center (RC), as seen in Fig. 2(b). Due to the symmetry of the electrodes and the conservation of power, the reflection coefficients of metal electrodes referred to their centers should be pure imaginary [12].

As seen in Fig. 2 (c), in either a DART or an EWC unit cell, a pair of electrodes with a width of $\lambda_0/8$ are connected to signal and ground with a pitch distance of $\lambda_0/4$. The acoustic waves respectively reflected by these electrodes have a phase difference of 180º at f_0 and interfere destructively. Assuming small reflections, their amplitudes can be considered equal, resulting in a perfect cancellation. In other words, acoustic waves reflected by the two adjacent $\lambda_0/8$ electrodes produce an overall zero reflection coefficient. As a result, the $\lambda_0/8$-wide electrodes with a center-to-center distance of $\lambda_0/4$ can be omitted from the analysis of reflections within the transducers. Different from the $\lambda_0/8$-wide electrodes, the wider electrodes are intended to produce pronounced reflections.

As seen in Fig. 1(b) and (c), the acoustic emission towards the acoustic port 2 is a combination of the waves generated at the TC towards Port 2 and the waves towards Port 3 that are reflected from the closest RC on the left. For both DART and EWC designs, the RCs are separated from TCs by a distance of $3\lambda_0/8$. Assuming a negative imaginary reflection coefficient Γ (with a phase angle of 90°), the reflected waves are in phase with the waves generated at the TC towards Port 2 (FWD port) at f_0. Note that the waves sent by the further cells on the left will also interfere constructively given the λ_0 periodicity. The acoustic emission towards Port 3 is the interference result of the waves generated at the TC and their reflection from the closest RC on the right. Due to the $5\lambda_0/8$ separation between the TCs

and the RCs on their right, the directly transduced waves towards Port 3 and their reflection from RCs are out of phase. Hence, acoustic port 3 (BWD port) receives smaller acoustic power than acoustic port 2 due to the partial cancellation of the directly transduced waves by the reflection. It is obvious that a single reflection is far from sufficient in achieving elimination of transduction towards Port 3 and uni-directionality towards Port 2. More unit cells are required for this purpose. In a multi-cell configuration, the RC in each cell will all serve to produce reflection for every TC. Therefore, the interference in both directions combine all the directly transduced waves from all TCs and all the reflections generated by all the RCs. The dynamics in a multi-cell configuration will be analyzed later in this section, and it will be shown that a near perfect uni-directionality is attainable with multiple cells and multi-reflections.

C. Analysis of Reflectors in Unidirectional Transducers

As discussed above, the directionality of an SPUDT is based on the reflectivity of the wide electrodes in each unit cell. Thus, prior to our discussion on the directionality of multi-cell SPUDT, the reflectivity of each reflector needs to be quantitatively modeled. The reflection coefficient Γ of an electrode can be considered as the result of two phenomena [12]. First, it has a mechanical component, Γ_m, caused by the edges of the electrode on the film, along with the change in the acoustic impedance in sections with metal coverage. The change in acoustic impedance arises from the unequal mass density and stiffness of the electrode metal and LiNbO$_3$. Second, Γ has an electrical contribution, Γ_e, caused by the constant potential boundary condition created on the top surface of the LiNbO$_3$ film by the metallization. In other words, Γ_e is the reflection coefficient created by a strip of perfect electric conductor (PEC) of zero thickness. To calculate the total reflection coefficient, we can treat the mechanical and electrical reflections as if they were produced at different locations separated by a distance x_0, as seen in Fig. 3. By solving the multiple reflections between these two locations and making $x_0 \to 0$, the total reflection coefficient is obtained as

$$\Gamma = \frac{\Gamma_e + \Gamma_m}{1 + \Gamma_e \Gamma_m}. \tag{3}$$

For small reflections, i.e. $\Gamma_e \Gamma_m \ll 1$, $\Gamma \approx \Gamma_e + \Gamma_m$.

The analytical expressions of mechanically induced reflections have been reported for SAW devices [39]. For wave propagation in plates, our method to predict the reflections from mechanical discontinuities relies on FEM simulations [36], [40]. For an electrode on a thin film, acoustic waves are reflected as they travel from an un-metalized section to a metalized portion of the LiNbO$_3$ film (step-up), and vice versa (step-down). As a result of both reflections, an equivalent overall mechanical reflection coefficient Γ_m can be defined for a single electrode. The model shown in Fig. 4(a) is built in Comsol to evaluate the mechanical reflection from the step-up discontinuity created by an electrode. The model consists of cascaded sections of the delay medium, non-metallized on one end and metallized on the other. Perfectly matched layer (PML) conditions are set at both
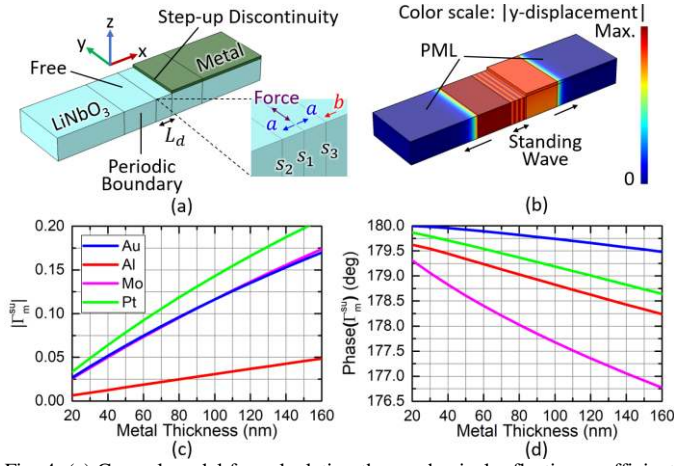
Fig. 4. (a) Comsol model for calculating the mechanical reflection coefficient from a step-up discontinuity caused by metallization. (b) Magnitude of y-axis displacement at 160 MHz. (c) Amplitude and (d) phase of the mechanical reflection coefficient as a function of metal thickness for different metals at 160 MHz. The thickness of the LiNbO$_3$ thin film is fixed at 800 nm in the analysis.

ends of the model to emulate an infinitely long mechanical medium extending along -x and +x. The cross-sectional planes normal to -y and +y are set as periodic boundaries. Following the method used in [41], acoustic waves are excited by a harmonic force applied to the cross section at x = 0, s_1 in Fig. 4(a), separated from the discontinuity by a distance L_d. With a y-axis excitation force, two SH0 waves a with the same amplitude are launched in the opposite directions, -x and +x. These two waves have opposite phases if we consider the strain ϵ_{xy} as the wave variable, and have the same phase if we consider the displacement, u_y. Fig. 4(b) shows the solution for the magnitude of u_y. A standing wave is created between s_1 and the metallization edge as a result of the interference of $a(x,t)$ with the reflected wave $b(x,t)$. A constant amplitude is observed between s_1 and the PML in the –x region, and between the discontinuity and the PML in the +x region. This indicates a perfect absorption of the acoustic power by the PMLs. The strain field ϵ_{xy} associated with the wave a can be written as

$$\epsilon_{xy}^a(x,t) = Ae^{-j\beta_\infty x}e^{j\omega t} \quad \text{for} \quad x > 0$$
$$\epsilon_{xy}^a(x,t) = -Ae^{j\beta_\infty x}e^{j\omega t} \quad \text{for} \quad x < 0, \tag{4}$$

where ω is the angular frequency and $\beta_\infty = \omega/v_\infty$ is the wavenumber in the un-metallized LiNbO$_3$ film. The strain field associated with the reflected wave b is then obtained as

$$\epsilon_{xy}^b(x,t) = Ae^{j\beta_\infty x}e^{-j\beta_\infty 2L_d}\Gamma_{su}e^{j\omega t} \quad \text{for} \quad x < L_d, \tag{5}$$

where the subscript su denotes the mechanical reflection coefficient associated with the step-up discontinuity. The stress at the cross-sections s_2 and s_3, separated from s_1 by a distance Δx [see Fig. 4(a)], can be obtained as the superposition of a and b waves at $x = -\Delta x$ and $x = \Delta x$, respectively:

$$\epsilon_{xy}^{s2}(t) = A(-e^{-j\beta_\infty \Delta x} + e^{-j\beta_\infty \Delta x}e^{-j\beta_\infty 2L_d}\Gamma_{su})e^{j\omega t} \tag{6}$$

$$\epsilon_{xy}^{s3}(t) = A(e^{-j\beta_\infty \Delta x} + e^{j\beta_\infty \Delta x}e^{-j\beta_\infty 2L_d}\Gamma_{su})e^{j\omega t}. \tag{7}$$

By making $\Delta x \to 0$, we attain the expression

$$\Gamma_{su} = \frac{u_y^b(x,t)}{u_y^a(x,t)} = -\frac{\epsilon_{xy}^b(x,t)}{\epsilon_{xy}^a(x,t)} = e^{-j\beta_\infty 2L_d}\frac{\epsilon_{xy}^{s3}+\epsilon_{xy}^{s2}}{\epsilon_{xy}^{s3}-\epsilon_{xy}^{s2}}. \tag{8}$$

where u_y^a and u_y^b are the displacements associated with the incident and reflected waves, respectively. Using this expression, the reflection coefficient Γ_{su} can then be easily obtained by evaluating ϵ_{xy}^{s2} and ϵ_{xy}^{s3} in the Comsol simulation. The procedure described above was performed for an 800 nm-thick LiNbO$_3$ film and four metals that are commonly used as electrodes in microsystems: gold (Au), aluminum (Al), molybdenum (Mo) and platinum (Pt). In all cases, a nearly constant Γ_{su} with frequency was found up to 500 MHz. At 160 MHz, the magnitude and phase of Γ_{su} are shown in Fig. 4(c) and (d) respectively as a function of the metal thickness. The magnitude of Γ_{su} is found to be nearly linearly dependent on the metal thickness. The phase is close to 180° for the simulated thickness range. The reflection coefficient of the electrode step-down, Γ_{sd}, is found to have the same magnitude but opposite phase ($\Gamma_{sd} = -\Gamma_{su}$). The overall mechanic reflection coefficient of an electrode can be found by summing the multiple reflections produced by the step-up and step-down discontinuities. Referencing the reflections to the center of the electrode, we attain the expression

$$\Gamma_m = \Gamma_{su}e^{j\alpha}\left(1 - e^{-j2\alpha}T_{su}\sum_{n=0}^{\infty}(\Gamma_{su}e^{-j\alpha})^{2n}\right) \tag{9}$$

where α is the phase retardation for traversing half the width of a reflector. α is $3\pi/4$ for DART and $\pi/2$ for EWC reflectors. T_{su} is the transmission coefficient of the step-up discontinuity,

$$T_{su} = 1 + \Gamma_{su}, \tag{10}$$

Introducing T_{su} to (9) and simplifying the geometric series, we obtain

$$\Gamma_m = \Gamma_{su}e^{j\alpha}\frac{1-e^{-j2\alpha}(1-\Gamma_{su}^2)}{1-\Gamma_{su}^2e^{-j2\alpha}}. \tag{11}$$

The electrical reflection can be calculated in a similar way by considering the change in phase velocity produced by the ground condition imposed by the reflector electrodes on top of the piezoelectric film. Similar to our approach with the mechanical reflection, we can define a reflection coefficient as the wave passes from an un-metalized to a metalized section,

$$\Gamma_{\infty 0} = \frac{v_0 - v_\infty}{v_0 + v_\infty}. \tag{12}$$

v_0 and v_∞ are the phase velocities for a piezoelectric medium with the free and electrically shorted top surfaces, respectively. The reflection coefficient as the wave passes from a metallized to an un-metallized section is $\Gamma_{0\infty} = -\Gamma_{\infty 0}$. The phase velocities of the SH0 mode are determined using finite element method (FEM) in Comsol. For an 800 nm-thick LiNbO$_3$ film, v_∞ is calculated to be 4507 m/s. For the same film with ground as the electrical boundary condition on the top surface, a v_0 of

3550 m/s is obtained. The overall electrical reflection coefficient of an electrode can be obtained following the same procedure as for (11),

$$\Gamma_e = \Gamma_{0\infty} e^{j\alpha} \frac{1 - e^{-j2\alpha}\left(1 - \Gamma_{0\infty}^2\right)}{1 - \Gamma_{0\infty}^2 e^{-j2\alpha}}. \tag{13}$$

Note that (13) does not consider the non-uniform electric fields created by the uneven charge distribution in an electrode when surrounded by other electrodes in an array or multi-cell configuration. An analytical method to calculate the electrical reflection accounting for this phenomenon can be found in [42]. However, this method assumes an array of electrodes with constant width and separation. Since this condition is not met by the reflectors in SPUDTs, the method will have to be revised in the future before being applied here.

　Based on Fig. 4, 100 nm-thick Au is chosen to implement the electrodes for enabling sufficient reflections and avoiding fabrication complications at the same time. For such a configuration, $\Gamma_{su} = -0.116$ is obtained if the imaginary part is neglected. Using (11), the mechanical reflection coefficients can be obtained for the wide electrodes in DART and EWC unit cells: $\Gamma_m^{DART} = -0.164$ j, $\Gamma_m^{EWC} = -0.229$ j. Regarding the electrical reflection, (12) results in $\Gamma_{\infty 0} = -0.119$, which, from (3), yields: $\Gamma_e^{DART} = -0.168$ j, $\Gamma_e^{EWC} = -0.235$ j. The total reflection coefficients, arising from both mechanical and electrical phenomena, can be obtained through (3) as $\Gamma^{DART} = -0.323$ j, $\Gamma^{EWC} = -0.440$ j. These values are negative imaginary as assumed in our analysis for RCs in the previous section. With electrodes of the same material and thickness, the reflection coefficients of reflectors in a SAW device on a YZ-LiNbO$_3$ substrate are at least one order of magnitude smaller [43]. As it will be shown in the next section, a higher reflectivity per reflectors will permit a higher uni-directionality in a multi-cell configuration. Considering that the BW of uni-directionality scales down as the number of unit cells increases, a higher reflectivity also implies a better tradeoff between delay line IL and BW.

D. Calculation of directionality

　As discussed earlier, multiple unit cells that are spaced by λ_0 in a cascaded configuration are typically required to attain highly uni-directional transduction. To be consistent with our framework used for analyzing a single cell, a multi-cell transducer is also considered with three ports, one electric port that is connected to all the cells for excitation, and two acoustic ports that are situated at the opposite ends of the multi-cell transducer. To quantitatively measure the directionality of multiple cells, a figure of merit dubbed as directionality of transduction is defined as

$$D = \frac{P_{FWD}}{P_{BWD}}, \tag{14}$$

where P_{FWD} is the power emitted towards the FWD port and P_{BWD} is the power emitted towards the BWD port. When a time harmonic voltage is applied at the electrical port, a transducer emits acoustic power towards both acoustic ports. The total emission to each port can be calculated as the superposition of
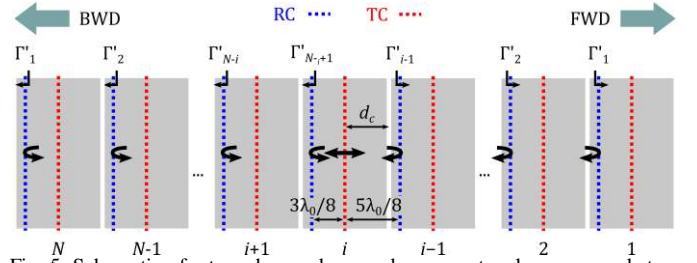

Fig. 5. Schematic of a transducer where each grey rectangle corresponds to a unit cell with marked RC and TC. For the ith unit cell, the directionality can be calculated by considering its TC and all the RCs at both sides.

the waves emitted by each TC in the transducer. To determine the power emitted by a single TC in a multi-cell configuration, a voltage source is connected to one TC at a time, while all other TCs are grounded.

　Fig. 5 shows the schematic of a SPUDT formed by N unit cells. As seen, the transduction center at the unit cell i has $i-1$ reflectors on its right (FWD) and $(N-i+1)$ reflectors on its left (BWD), with all reflectors featuring the same reflection coefficient, Γ. Each RC in the transducer is denoted by an index k. At the $(i-1)^{th}$ RC which is on the immediate right of the ith TC (i.e., $k = i-1$), we define an equivalent reflection coefficient Γ_k' that accounts for all the reflections produced by the unit cells from 1 to k. For $k=1$, this is simply $\Gamma_1' = \Gamma$. For $k=2$, the equivalent reflection coefficient must account for the multiple reflections between the RCs of unit cells 1 and 2. At f_0, there is a 2π phase separation between the RCs, giving:

$$\Gamma_2' = \Gamma + T^2 \Gamma_1' \sum_{n=0}^{\infty} \left(\Gamma_1' \Gamma\right)^n \tag{15}$$

where T is the transmission coefficient of the RCs, and can be obtained as:

$$T = \frac{1 - \Gamma_{\infty m}^2}{1 - \Gamma_{\infty m}^2 e^{-j2\alpha}}, \tag{16}$$

where $\Gamma_{\infty m} = (\Gamma_{su} + \Gamma_{\infty 0})/(1 + \Gamma_{su}\Gamma_{\infty 0})$ is the total reflection experienced by a wave traveling from an un-metallized to a metallized section. By substituting (16) into (15) and simplifying the geometric series, (15) is reduced to

$$\Gamma_2' = \Gamma + \frac{T\,\Gamma}{1 - \Gamma^2}. \tag{17}$$

This method can be applied to the successive RCs, leading to the recursive definition of Γ_k':

$$\Gamma_k' = \Gamma + \frac{T\,\Gamma_{k-1}'}{1 - \Gamma\,\Gamma_{k-1}'} \tag{18}$$

The equivalent reflection coefficients of the RCs on the left of the ith TC can be obtained in the same way from the right to the left as Γ_{N-k+1}' (see Fig. 5). Referencing to Γ_k', we can define equivalent transmission coefficients of each RC:

$$T_k' = e^{j\phi_k}\sqrt{1 - |\Gamma_k'|^2}, \tag{19}$$

where ϕ_k is the phase of the transmission coefficient. Then, the directionality of unit cell i can be calculated by attending the ith

TC with two overall reflections aggregated at the two adjacent RCs on the left and right, with reflection coefficients Γ'_{N-i+1} and Γ'_{i-1} respectively. By solving the multiple reflections for the two waves generated at the TC in the opposite directions, the wave amplitude emitted to the FWD port can be derived as

$$a_i^{FWD} = \psi \frac{e^{-j(3\pi/4-\phi_{i-1})}\sqrt{1-|\Gamma'_{i-1}|^2}(e^{-j\pi/2}+\Gamma'_{N-i+1})}{1-\Gamma'_{i-1}\Gamma'_{N-i+1}}, \qquad (20)$$

where ψ is the transduction coefficient. For the wave radiated to the BWD port, we get

$$a_i^{BWD} = \psi \frac{e^{-j(3\pi/4-\phi_{N-i+1})}\sqrt{1-|\Gamma'_{N-i+1}|^2}(1+e^{-j\pi/2}+\Gamma'_{i-1})}{1-\Gamma'_{i-1}\Gamma'_{N-i+1}} \qquad (21)$$

Imposing that, from (18), all the Γ'_k are negative imaginary, the directionality of the unit cell i is obtained as

$$D_i = \frac{|a_i^{FWD}|^2}{|a_i^{BWD}|^2} = \frac{\left(1+|\Gamma'_{i-1}|\right)\left(1+|\Gamma'_{N-i+1}|\right)}{\left(1-|\Gamma'_{i-1}|\right)\left(1-|\Gamma'_{N-i+1}|\right)}. \qquad (22)$$

By evaluating (18) into (22), it can be proven that the directionality of each unit cell in a multi-cell configuration has the same value

$$D_i = \left(\frac{1+|\Gamma|}{1-|\Gamma|}\right)^N, \qquad (23)$$

which, by linear superposition, is also the overall directionality of the whole transducer, D. The transducer directionality calculated in this way is plotted in Fig. 6 as a function of the number of cells, for different values of the reflection coefficient. The specific values calculated above for the DART and EWC, $\Gamma^{DART} = -0.204\,\text{j}$ and $\Gamma^{EWC} = -0.359\,\text{j}$, are represented by solid lines. If (3) is introduced in (23), the directionality is obtained as a composition of two factors, the directionality due to the electrical reflection, D_e, and the directionality due to the mechanical reflection, D_m:

$$D = D_e\,D_m = \left(\frac{1+|\Gamma_e|}{1-|\Gamma_e|}\right)^N \left(\frac{1+|\Gamma_m|}{1-|\Gamma_m|}\right)^N \qquad (24)$$

E. Estimate of Group Delay

The group delay of a delay line employing the abovementioned transducers is challenging to precisely predict with a closed form expression. This is due to the complexity introduced by the multiple reflections between the different cells in each transducer. A simplified analysis can be done by disregarding these internal reflections. Consider the transfer function $F(\omega)$ from the input port to the center of the delay line in Fig. 1(a). It can be expressed as the superposition of the phase-retarded N waves generated by the unit cells. Assuming lossless propagation, each term in $F(\omega)$ has three phase delay components: the first one due to the propagation over a distance d_c from the TC to the right edge of each unit cell [see Fig. 5], the second one from the right edge of each unit cell to the right edge of the entire input transducer, and the third one from the right edge of the input transducer to the center of the delay line over a distance $L_G/2$. $F(\omega)$ can be then expressed as:
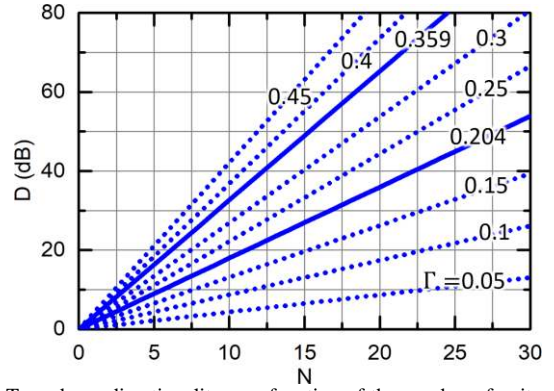

Fig. 6. Transducer directionality as a function of the number of unit cells (N) for different values of the overall reflection coefficient (Γ). The solid lines correspond to the reflection coefficients derived for DART and EWC reflectors of 100 nm-thick Au.

$$F(\omega) = \sum_{n=1}^{N} e^{-j(\beta_t d_c + \beta_t \lambda_0 (n-1) + \beta_\infty L_G/2)} \qquad (25)$$

where $\beta_t = \omega/v_t$ is the average wave number within the unit cell. The phase of $F(\omega)$ can be calculated using the expression in [44] and Euler's identity:

$$\angle F(\omega) = -\frac{\omega L_G}{2v_\infty} - \frac{\omega d_c}{v_t} - \arctan\left(\frac{\sin(N\lambda_0\omega/v_t)}{\cos(N\lambda_0\omega/v_t)-1}\right) \\ + \arctan\left(\frac{\sin(\lambda_0\omega/v_t)}{\cos(\lambda_0\omega/v_t)-1}\right). \qquad (26)$$

By reciprocity and symmetry of the transducers, this is also equal to the phase shift experienced by a signal from the center of the delay line to the output port. Thus, the total group delay at f_0 can be obtained as

$$\tau_g(f_0) = -2\frac{d\angle F(\omega)}{d\omega}\bigg|_{\omega=\omega_0} = \frac{L_G}{v_\infty} + \frac{2d_c}{f_0\lambda_0} + \frac{N-1}{f_0}. \qquad (27)$$

The first term is the delay introduced by the gap L_G between transducers. The second and third terms correspond to the delays from the wave propagation within the transducers.

III. MODELING AND SIMULATION

A Comsol-based FEM model of a unidirectional transducer was built to more precisely predict the directionality as a function of the number of unit cells. The directionality per unit cell was simulated for an EWC transducer formed by 100 nm of Au for different values of N. The results are shown in Fig. 7 (red curve). Theoretically, this value can be predicted from (23) as

$$D/N \text{ (dB)} = 10\log\left(\frac{1+|\Gamma|}{1-|\Gamma|}\right). \qquad (28)$$

Note that, different from (28), the simulated D/N shows a dependence on N for low values of N. This can be explained by the fringe effects in the transducer, which makes the unit cells close to the edges present a smaller directionality than those cells located in the middle of the transducer. To gain insight into this phenomenon, additional simulations were performed. In the first simulation, represented by the blue curve in Fig. 7, zero thickness electrodes were used to obtain the directionality due
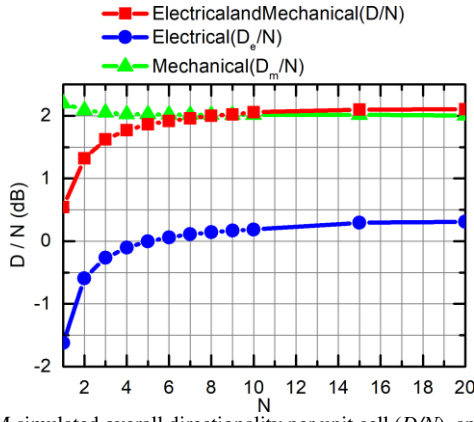
Fig. 7. FEM simulated overall directionality per unit cell (*D/N*), and calculated directionality per unit cell due to electrical (*D_e/N*) and mechanical (*D_m/N*) reflections.
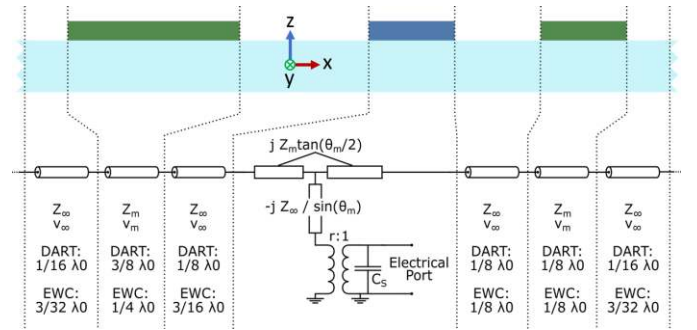

Fig. 8. Sectional Mason's model for a single unit cell. Each uniform portion of the unit cell is represented by an acoustic transmission-line section. The acoustic impedance, phase velocity, and length of each section are labelled with symbols.

to electrical reflections, D_e. In another case, represented by the green curve in Fig. 7, a pure solid mechanical simulation was performed, disregarding the piezoelectricity, to obtain the directionality due to the mechanical reflections, D_m. The excitation was done by applying harmonic y-axis forces to the signal electrodes. From these results, it is clear that the mechanical reflections are dominant for high values of N. Moreover, the fringe effects mainly pertain to the electrical part of the reflections due to the distorted electric field distribution near the transducer edges. Finally, the electrical reflection coefficient approximated by (13) is overestimated. A directionality of 2.1 dB per unit cell is deduced for EWC transducers with many cells. The total reflection coefficient can be indirectly obtained from (28) as $|\Gamma^{EWC}| = 0.24$. With the same method, the reflectors in DART transducers show $|\Gamma^{DART}| = 0.17$.

In order to predict the response of the described ADLs with intricacies that are omitted in the closed-form analysis, an equivalent circuit model was used. This method, based on Mason's model, employs a 1D discretization of the delay line by representing each unit cell of the transducers with a sectional equivalent circuit. The schematic of the implemented model for a single unit cell can be found in Fig. 8. Following the procedure described in [45], each section with uniform properties is modeled by a transmission line. The phase velocities for the unmetalized and metalized sections were calculated in Comsol as $v_\infty = 4507$ m/s and $v_m = 2958$ m/s. The reflections due to the discontinuities are modelled by the different characteristic impedances of the sections representing metallized and unmetallized LiNbO$_3$, respectively Z_m and Z_∞. The ratio can be calculated as

$$\frac{Z_m}{Z_\infty} = \frac{1+\Gamma_{\infty m}}{1-\Gamma_{\infty m}}, \tag{29}$$

where $\Gamma_{\infty m}$ is the reflection coefficient for an acoustic wave passing from un-metallized to metallized LiNbO$_3$. The reflection coefficient of an electrode can be approximated as a sum of two reflections at the step-up and step-down discontinuities, assuming small reflections. Given the width of the reflectors, these reflections are in quadrature for DART and in phase for EWC. Thus, it can be deduced that

$$\Gamma_{\infty m}^{DART} = \frac{1}{\sqrt{2}}\left|\Gamma^{DART}\right|, \tag{30}$$

$$\Gamma_{\infty m}^{EWC} = \frac{1}{2}\left|\Gamma^{EWC}\right|. \tag{31}$$

The lengths of the transmission line sections are labeled in Fig. 8 for both the DART and EWC designs. The transduction section, which includes the signal electrode, is modeled as a T-shaped network with an ideal transformer connecting to the electrical port. The transformation ratio is determined by the electromechanical coupling and is given by

$$r = \sqrt{2\pi f_0 C_s k^2 Z_m}, \tag{32}$$

where C_s represents the static capacitance per unit cell. From an electrostatic simulation in Comsol, $C_s/W_A = 250$ aF/μm was calculated for an 800 nm-thick LiNbO$_3$ film, where W_A is the acoustic aperture [see Fig. 1(a)]. The value for the electromechanical coupling k^2 is assumed 40% [35]. Note the ratio Z_m/Z_∞ defines the reflections, but the value of Z_∞ (or Z_m) is irrelevant for the electric response. Hence, $Z_\infty = 1$ is taken. The angle θ_m can be obtained as

$$\theta_m = \frac{\pi}{4}\frac{f\lambda_0}{v_m} \tag{33}$$

for both DART and EWC transducers.

With all the parameters defined, a model for a complete transducer can be built by concatenating the models of its unit cells. The unit cells must be connected in series in the acoustic domain, and in parallel in the electrical domain to form the electrical port of the transducer. A complete delay line can be simulated by connecting the models of two transducers in the acoustic domain with their FWD ports facing each other. The gap between the transducers can be modeled by an acoustic transmission line with characteristic impedance Z_∞, phase velocity v_∞ and length L_G. To ensure no reflection at the BWD ports of both transducers, these must be terminated by an impedance Z_∞.

A Comsol model of an entire ADL was also built to validate the circuit model. Fig. 9(a) shows the 3D model for a device with EWC transducers that have $N = 10$, $\lambda_0 = 20$ μm, $W_A = 200$ μm, and $L_G = 120$ μm. Fig. 9(b) presents the solution for the magnitude of the displacement along the y-axis at f_0, The
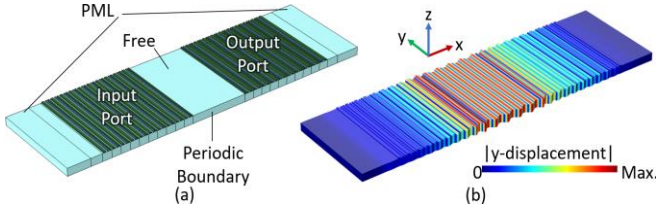
Fig. 9. (a) FEM model built in Comsol to simulate the response of the ADLs. (b) Displacement magnitude along the y-axis at the center frequency.

TABLE I
DESIGN PARAMETERS OF THE FABRICATED ACOUSTIC DELAY LINES

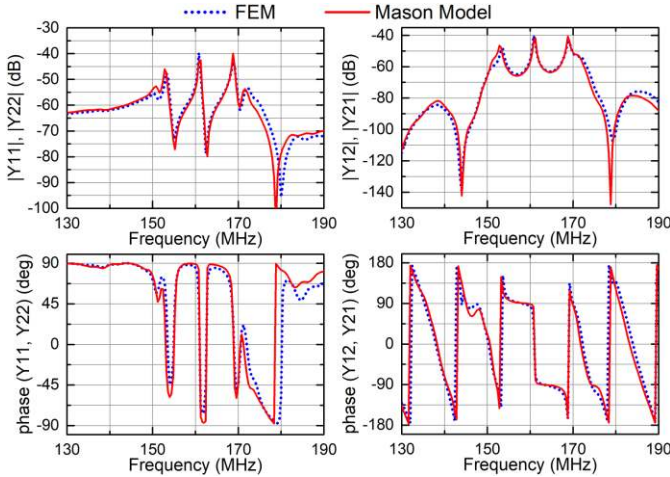| ID	Type of Transducers	N	L_G (μm)	λ_0 (μm)	W_A (μm)	τ_g (ns)
1	DART	10	120	20	200	79
2	DART	10	500	20	200	164
3	DART	10	1000	20	200	274
4	DART	15	120	20	200	106
5	DART	15	500	20	200	190
6	DART	20	120	20	200	132
7	DART	20	500	20	200	217
8	EWC	10	120	20	200	79
9	EWC	10	1000	20	200	274
10	EWC	15	120	20	200	106
11	EWC	20	120	20	200	132
12	EWC	20	1500	20	200	439
13	DART/Bid (FWD)	10	120	20	200	
14	DART/Bid (BWD)	10	120	20	200	
15	EWC/Bid (FWD)	10	120	20	200	
16	EWC/Bid (BWD)	10	120	20	200	

Fig. 10. Simulated Y-parameters using the FEM and Mason's models. Both models assume zero propagation loss in the delay line.

Y-parameters are computed using both FEM and Mason's models and the results are shown in Fig. 10. An excellent match has been achieved between the two models. Note that these models do not consider any dissipative loss in the device structure.

IV. DEVICE DESIGNS AND FABRICATION

Guided by the reflectivity analysis presented in Section II, Au was chosen as the material for the electrodes, with a thickness of 100 nm. An X-cut LiNbO$_3$ thin film of 800 nm is chosen as the propagation medium since high coupling and low loss for SH0 waves have been previously demonstrated in this platform [35]. The propagation direction, namely along the x-axis in Fig. 1(a), was chosen as -10° with respect to the +Y crystallographic axis of LiNbO$_3$ to maximize k^2 [46], [47]. Table I lists the parameters of the implemented designs. Devices 1-12 are meant to sweep the main design parameters as a way to characterize the propagation loss in the LiNbO$_3$ film, as well as the loss associated with the transducers, for constant center frequency and acoustic aperture. The expected group delays according to (27) are also listed in Table I. Devices 13-16 are test structures to characterize the directionality of DART and EWC transducers formed by 10 cells. These devices are formed by a SPUDT transducer and a bi-directional transducer with regular-width electrodes. In the bidirectional transducer, each period of λ_0 contains 4 electrodes of $\lambda_0/8$ width to minimize reflections. The electrodes are connected in the sequence of 'ground-ground-signal-signal' to have the same center frequency as the SPUDT. In addition, both transducers are of the same length for

attaining similar bandwidths. In Devices 13 and 15, the FWD ports of the SPUDTs are facing the bidirectional transducers. In Devices 14 and 16, the BWD ports of the SPUDTs are facing the bidirectional transducers.

The sixteen devices listed in Table I were fabricated on a single chip with the process depicted in Fig. 11. The film transfer process involves two steps. In the first step, an X-cut LiNbO$_3$ wafer is bonded to a Si carrier wafer. Second, the bonded LiNbO$_3$ layer is thinned down to a thickness of 800 nm. Next, the 100 nm-thick Au electrodes are defined with sputter-deposition and lift-off. Then, the release windows must be defined. For this purpose, a 1 μm-thick hard mask of SiO$_2$ is created by plasma enhanced chemical vapor deposition (PECVD) and is patterned with fluorine-based reactive ion etching (RIE). The release windows in the LiNbO$_3$ film are subsequently etched by chlorine-based inductive coupled plasma (ICP)-RIE before the SiO$_2$ is removed with a buffered oxide etch (BOE). To prevent the Au electrodes from being exposed to XeF$_2$ and etched in the device release step, a photoresist (PR) is spun and patterned to protect the electrodes and leave the release windows exposed. The devices are then released by isotropic XeF$_2$ etching, and the PR is removed with acetone. Fig. 11(b) and (c) show the optical pictures of two of the fabricated devices with electrode patterns exhibiting a great fidelity to the designs.

V. EXPERIMENTAL RESULTS AND DISCUSSIONS

The S-parameters of all the fabricated devices were characterized using a Keysight performance network analyzer PNA-X N5249A at room temperature. The measured data is then normalized to a matching complex port impedance in ADS to extract the IL over the transmission bands. In implementation, the impedance matching to 50 Ω can be done with an LC matching network with sufficient bandwidth, such as the one shown in [17]. The delay lines reported here present bandwidths under 15%. Matching networks with LC circuits can be readily implemented to cover such bandwidths, given the high k^2 of the SH0 waves in LiNbO$_3$ thin-films [35].

A. Measured Directionality of SPUDT

Fig. 12 shows the optical pictures of the fabricated Devices
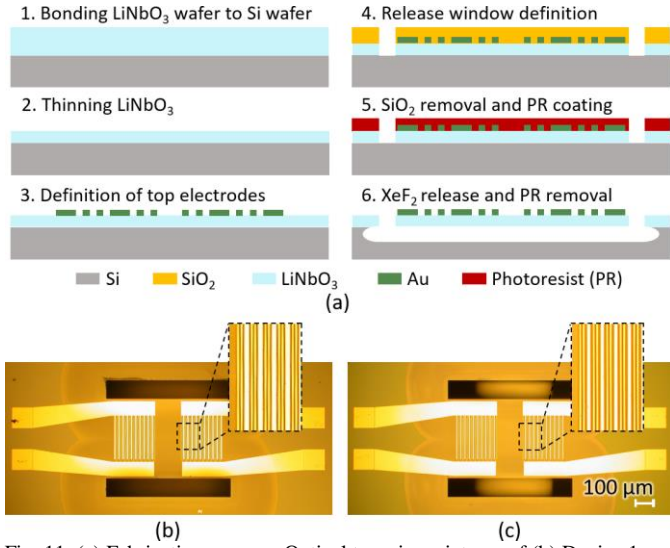
Fig. 11. (a) Fabrication process. Optical top-view pictures of (b) Device 1 and (c) 8.
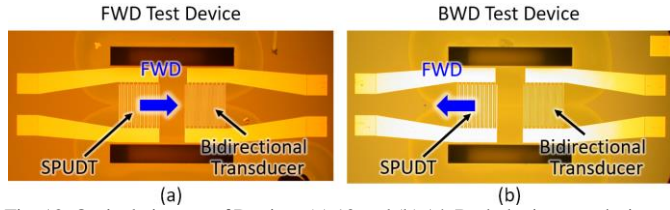

Fig. 12. Optical pictures of Devices (a) 13 and (b) 14. Both devices are designed to test the directionality of the DART SPUDT for SH0 waves in LiNbO₃.
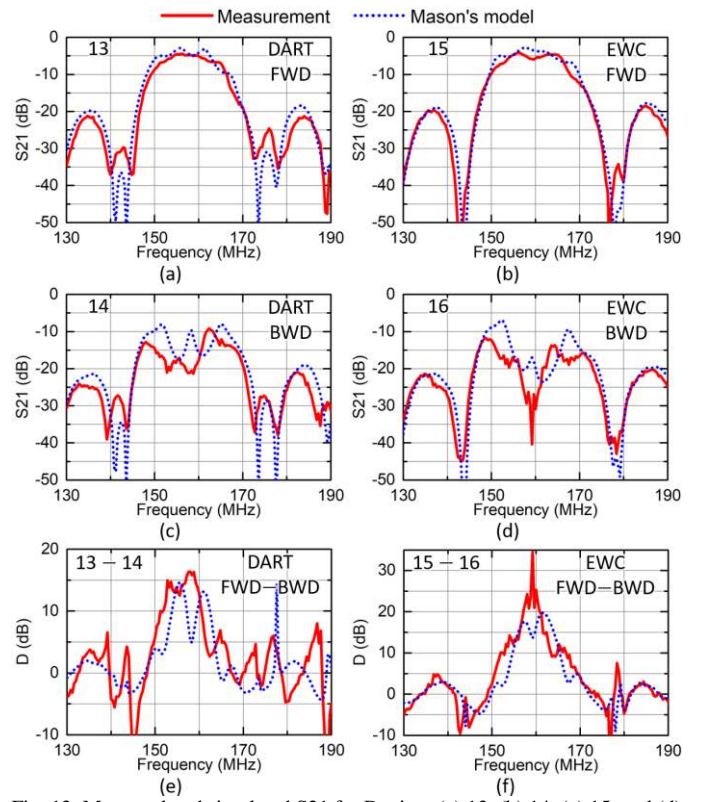

Fig. 13. Measured and simulated S21 for Devices (a) 13, (b) 14, (c) 15, and (d) 16. Measured and simulated directionality of the (e) DART and (f) EWC transducers with 10 unit cells. The directionality is deemed as the difference in measured and simulated S21 between FWD and BWD devices.

13 and 14, which are meant for testing the directionality of SPUDTs. The measured S21 with normalization to matched port impedances is shown in Fig. 13 for Devices 13 and 14 with the DART design, and for devices 15 and 16 with the EWC design. In both cases, the directionality of the SPUDT can be obtained by subtracting the S21 of the BWD devices from the S21 of the FWD devices. For the DART transducer with 10 unit cells, the measurements show a maximum directionality of about 15 dB. For the EWC, the directionality reaches more than 20 dB at the center frequency. Both values are in reasonable agreement with the analytical model (Fig. 7) and FEM simulation.

B. Measured IL and Group Delay

Among the fabricated devices, Devices 1 and 8, that use DART and EWC transducers respectively, present the lowest IL. Their S-parameters are plotted in Fig. 14, along with their group delays. The simulated S-parameters and calculated group delays according to (27) are also plotted. Both devices show a minimum IL around 2 dB. In spite of the low reflectivity of SPUDT transducers when their electrical ports are matched [38], ripples with amplitudes of about 1 dB can be observed in the passbands of both devices. The ripples make it challenging to compare the IL of different devices and evaluate the loss contributions from different loss mechanisms. In order to overcome this issue, the measured S21 results were fitted by the following expression:

$$S21 = a_1 \, \text{sinc}^2\left(a_2 \frac{f - a_3}{a_3}\right) \qquad (34)$$

which has been previously derived to describe the transmission band of a piezoelectric delay line with no reflections between the transducers [48].

The maximum S21 values of the fitting curves are then considered as the IL of the measured devices for the purpose of comparison. This procedure is performed for devices 1-12, and the resulting IL values are shown in Fig. 15. Data points for devices with the same transducer type and N are connected by straight dashed lines.

Two general trends are observed in Fig. 15. First, IL is larger for a longer delay line with the same number of unit cells. Second, IL increases as more transducer unit cells are used for a delay line of the same length. In other words, Fig. 15 indicates that the IL obtained for each device can be attributed to two distinctive causes. First, there is loss due to the propagation through the separation (L_G) between the input and out transducers, which will be denoted as IL_p. The second loss component is caused by the transducers, IL_t, which corresponds to the interception points of the lines with the y-axis in Fig. 15.

The IL_p can be straightforwardly extracted as the slope of the lines in Fig. 15. An average value of IL_p of 1.19 dB/mm is extracted from all the lines. From (27), it can be seen that the separation is responsible for a delay of 222 ns/mm. Therefore, we can express IL_p per unit delay: IL_p=5.8 dB/µs.
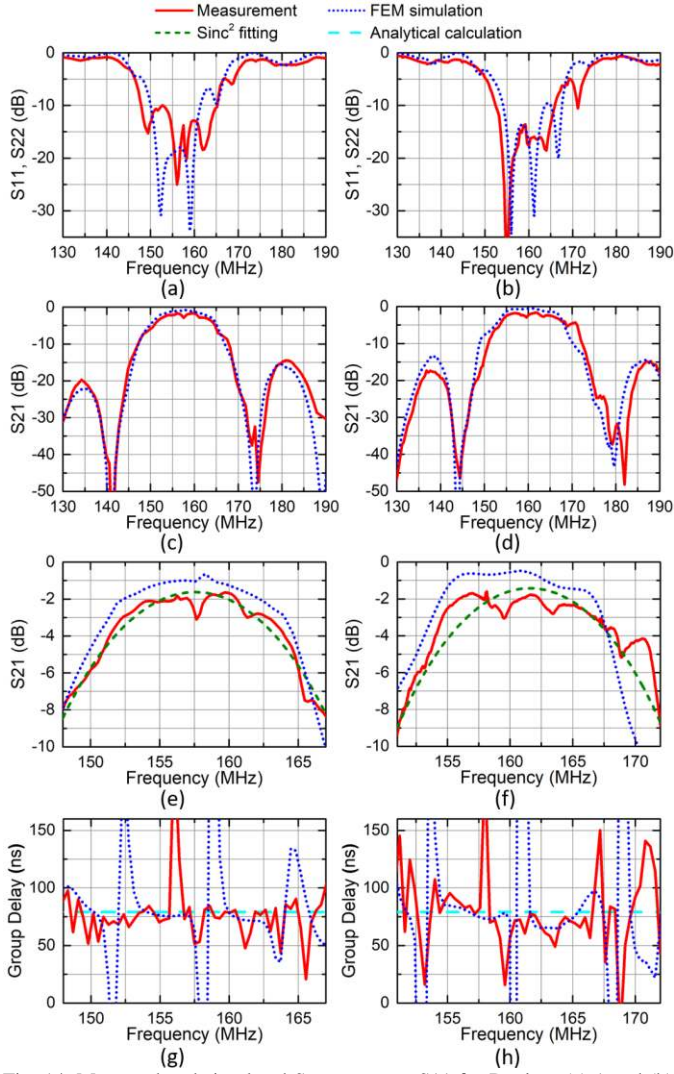
Fig. 14. Measured and simulated S-parameters. S11 for Devices (a) 1 and (b) 8. S21 for Devices (c) 1 and (d) 8. Zoom-ins of S21, showing comparison between the measurements and the fitting curves for Devices (e) 1 and (f) 8. Measured and simulated group delays for Devices (g) 1 and (h) 8. The analytically calculated delay based on (27) is also shown in (g) and (h) for comparison.
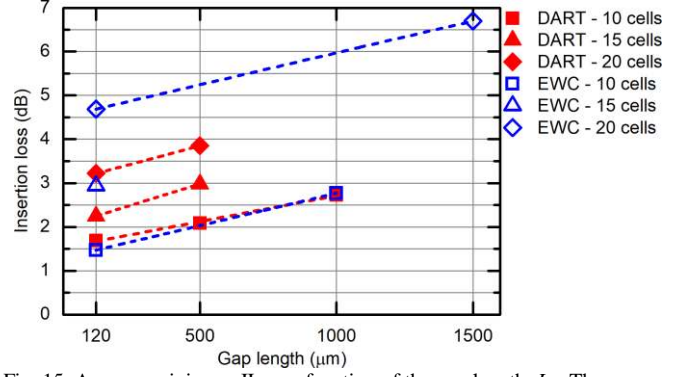

Fig. 15. Average minimum IL as a function of the gap length, L_G. The average minimum IL is obtained by fitting the measured response of each device with (34).
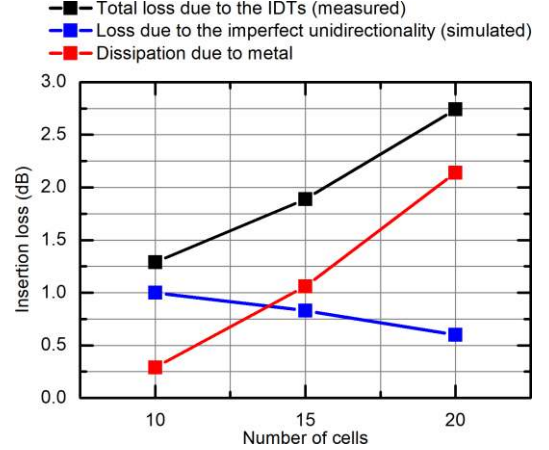

Fig. 16. Loss break-down in the transducers (input and output) including the total loss due to the transducers (extracted from the measurements) and the loss due to imperfect unidirectionality (calculated from simulation) for devices 1, 4, and 6. The difference between them allows for obtaining the dissipation due to metal.

On the other hand, the IL_t is more complex to analyze. As shown in Section II, the transducer directionality is predicted to grow with the number of cells in the transducers, enabling delay lines with decreasing IL_t as N increases. However, the trend seen in measurements, which shows IL_t increases with N, contradicts the theoretical prediction. This suggests a second transducer loss component that also scales with the number of unit cells, and is more dominant than the loss due to imperfect unidirectionality. This loss can possibly come from the dissipation at the electrode and piezoelectric interface, thermoelastic damping (TED), acoustic attention in the metal, or a combination of the above. Unfortunately, it is challenging to separate the dissipative loss component caused from the loss given by the imperfect unidirectionality in measurements due to the ripples. However, the latter can be indirectly estimated from FEM simulation. Fig. 16 shows the total loss in the transducers, IL_t for ADLs formed by DART transducers of 10, 15, and 20 unit cells

with the same L_G and W_A. The loss from imperfect unidirectionality, which is derived from simulation in Comsol, is also plotted. The remainder of the IL can then be attributed to the dissipative effects associated with the metal electrodes.

From the analysis shown in Fig. 16, it can be concluded that the IL of a device formed by either DART or EWC transducers of 10 cells can be expressed as

$$IL \text{ (dB)} = 1.29 + 5.8\, \tau_g(\mu s). \qquad (35)$$

To further minimize IL, a more optimal trade-off between the acoustic reflectivity and TED should be explored by resorting to other metals as electrode materials. The 3 dB FBW is 9% for Device 1 and 12% for Device 8. In comparison, the EWC design achieves a slightly higher bandwidth with comparable IL.

VI. CONCLUSIONS

A new type of acoustic delay lines has been demonstrated based on shear-horizontal waves propagating in a thin film of LiNbO₃. Analyses of the acoustic reflections have shown the promising prospects of this platform for building transducers with large unidirectionality. The results show that group delays of tens of ns can be achieved with a low IL of 2 dB and a FBW in excess of 10%. These devices open new possibilities for wide

band acoustic signal processing for compact low-power RF applications.

References

[1] R. H. Olsson, R. B. Bogoslovov, and C. Gordon, "Event driven persistent sensing: Overcoming the energy and lifetime limitations in unattended wireless sensors," *Proc. IEEE Sensors*, pp. 3–5, 2017.

[2] E. J. Barlow, "Doppler Radar," *Proc. IRE*, vol. 37, no. 4, pp. 340–355, Apr. 1949.

[3] M. A. C. S. Brown, W. J. Hannis, J. M. Skinner, and D. K. Turton, "Use of a surface-acoustic-wave delay line to provide pseudocoherence in a clutter-reference pulse Doppler radar," *Electron. Lett.*, vol. 9, no. 2, p. 17, 1973.

[4] P. F. Blomley and J. N. Gooding, "A S.A.W. Frequency Discriminator," in *1973 Ultrasonics Symposium*, 1973, pp. 468–471.

[5] C. L. Grasse and D. A. Gandolfo, "Acoustic Surface Wave Dispersive Delay Lines as High Resolution Frequency Discriminator," in *1972 Ultrasonics Symposium*, 1972, vol. 24, pp. 233–236.

[6] H.-S. Kao, M.-J. Yang, and T.-C. Lee, "A Delay-Line-Based GFSK Demodulator for Low-IF Receivers," in *2007 IEEE International Solid-State Circuits Conference. Digest of Technical Papers*, 2007, pp. 88–589.

[7] S. A. Reible, J. H. Cafarella, R. W. Ralston, and E. Stern, "Convolvers for DPSK Demodulation of Spread Spectrum Signals," in *1976 Ultrasonics Symposium*, 1976, pp. 451–455.

[8] D. C. Malocha, D. Puccio, and D. Gallagher, "Orthogonal frequency coding for SAW device applications," in *IEEE Ultrasonics Symposium, 2004*, 2004, vol. 2, no. c, pp. 1082–1085.

[9] T. Manzaneque, R. Lu, Y. Yang, and S. Gong, "An SH0 lithium niobate correlator for orthogonal frequency coded spread spectrum communications," in *2017 Joint Conference of the European Frequency and Time Forum and IEEE International Frequency Control Symposium (EFTF/IFC)*, 2017, pp. 143–147.

[10] R. Weigel, D. P. Morgan, J. M. Owens, A. Ballato, K. M. Lakin, K. Hashimoto, and C. C. W. Ruppel, "Microwave acoustic materials, devices, and applications," *IEEE Trans. Microw. Theory Tech.*, vol. 50, no. 3, pp. 738–749, Mar. 2002.

[11] H. E. Kallmann, "Transversal Filters," *Proc. IRE*, vol. 28, no. 7, pp. 302–310, Jul. 1940.

[12] D. Morgan, *Surface Acoustic Wave Filters: With Applications to Electronic Communications and Signal Processing*. Elsevier Science, 2010.

[13] R. H. Tancrell and M. G. Holland, "Acoustic surface wave filters," *Proc. IEEE*, vol. 59, no. 3, pp. 393–409, Jan. 1971.

[14] T. Takai, H. Iwamoto, Y. Takamine, H. Yamazaki, T. Fuyutsume, H. Kyoya, T. Nakao, H. Kando, M. Hiramoto, T. Toi, M. Koshino, and N. Nakajima, "High-Performance SAW Resonator on New Multilayered Substrate Using LiTaO 3 Crystal," *IEEE Trans. Ultrason. Ferroelectr. Freq. Control*, vol. 64, no. 9, pp. 1382–1389, Sep. 2017.

[15] Songbin Gong and G. Piazza, "Monolithic Multi-Frequency Wideband RF Filters Using Two-Port Laterally Vibrating Lithium Niobate MEMS Resonators," *J. Microelectromechanical Syst.*, vol. 23, no. 5, pp. 1188–1197, Oct. 2014.

[16] R. C. Ruby, P. Bradley, Y. Oshmyansky, A. Chien, and J. D. Larson, "Thin film bulk wave acoustic resonators (FBAR) for wireless applications," in *2001 IEEE Ultrasonics Symposium. Proceedings. An International Symposium (Cat. No.01CH37263)*, 2001, vol. 1, pp. 813–821.

[17] R. Lu, T. Manzaneque, Y. Yang, A. Gao, L. Gao, and S. Gong, "A Radio Frequency Non-reciprocal Network Based on Switched Low-loss Acoustic Delay Lines," *arXiv Prepr. arXiv1801.03814*, 2018.

[18] R. Lu, J. Krol, L. Gao, and S. Gong, "Frequency Independent Framework for Synthesis of Programmable Non-reciprocal Networks," *arXiv Prepr. arXiv1801.01548*, 2018.

[19] M. M. Biedka, R. Zhu, Q. M. Xu, and Y. E. Wang, "Ultra-Wide Band Non-reciprocity through Sequentially-Switched Delay Lines," *Sci. Rep.*, vol. 7, no. January, p. 40014, Jan. 2017.

[20] T. Dinc, M. Tymchenko, A. Nagulu, D. Sounas, A. Alu, and H. Krishnaswamy, "Synchronized conductivity modulation to realize broadband lossless magnetic-free non-reciprocity," *Nat. Commun.*, vol. 8, no. 1, pp. 1–9, 2017.

[21] C. Vezyrtzis, W. Jiang, S. M. Nowick, and Y. Tsividis, "A Flexible, Event-Driven Digital Filter With Frequency Response Independent of Input Sample Rate," *IEEE J. Solid-State Circuits*, vol. 49, no. 10, pp. 2292–2304, Oct. 2014.

[22] H. Scherr, G. Scholl, F. Seifert, and R. Weigel, "Quartz pressure sensor based on SAW reflective delay line," *1996 IEEE Ultrason. Symp. Proc.*, vol. 1, no. 2, pp. 347–350, 1996.

[23] J. H. Collins, H. M. Gerard, T. M. Reeder, and H. J. Shaw, "Unidirectional surface wave transducer," *Proc. IEEE*, vol. 57, no. 5, pp. 833–835, 1969.

[24] C. S. Hartmann, W. S. Jones, and H. Vollers, "Wideband Unidirectional Interdigital Surface Wave Transducers," *IEEE Trans. Sonics Ultrason.*, vol. 19, no. 3, pp. 378–380, Jul. 1972.

[25] R. C. Rosenfeld, R. B. Brown, and C. S. Hartrnann, "Unidirectional Acoustic Surface Wave Filters with 2 dB Insertion Loss," in *1974 Ultrasonics Symposium*, 1974, pp. 425–428.

[26] T. Kodama, H. Kawabata, H. Sato, and Y. Yasuhara, "Design of low–loss saw filters employing distributed acoustic reflection transducers," *Electron. Commun. Japan (Part II Electron.*, vol. 70, no. 9, pp. 32–44, 1987.

[27] V. B. Chvets, P. G. Ivanov, V. M. Makarov, and V. S. Orlov, "Low-loss SAW filters using new SPUDT structures," in *1997 IEEE Ultrasonics Symposium Proceedings. An International Symposium (Cat. No.97CH36118)*, 1997, vol. 1, pp. 69–72.

[28] Ventura, Solal, Dufilie, Hode, and Roux, "A new concept in SPUDT design: the RSPUDT (resonant SPUDT)," in *Proceedings of IEEE Ultrasonics Symposium ULTSYM-94*, 1994, vol. 1, pp. 1–6 vol.1.

[29] P. V. Wright, "The Natural Single-Phase Unidirectional Transducer: A New Low-Loss SAW Transducer," in *IEEE 1985 Ultrasonics Symposium*, 1985, pp. 58–63.

[30] C. S. Hartmann, P. V. Wright, R. J. Kansy, and E. M. Garber, "An Analysis of SAW Interdigital Transducers with Internal Reflections and the Application to the Design of Single-Phase Unidirectional Transducers," in *1982 Ultrasonics Symposium*, 1982, pp. 40–45.

[31] R. B. Brown, "Electrical Matching of Unidirectional Surface Wave Devices," in *MTT-S International Microwave Symposium Digest*, vol. 75, no. 0, pp. 359–361.

[32] K. Yamanouchi and H. Furuyashiki, "Low-loss SAW filter using internal reflection types of single-phase unidirectional transducer," *Electron. Lett.*, vol. 20, no. 20, p. 819, 1984.

[33] S. Gong, L. Shi, and G. Piazza, "High electromechanical coupling MEMS resonators at 530 MHz using ion sliced X-cut LiNbO3thin film," *IEEE MTT-S Int. Microw. Symp. Dig.*, no. August, pp. 29–32, 2012.

[34] S. Gong and G. Piazza, "Design and Analysis of Lithium–Niobate-Based High Electromechanical Coupling RF-MEMS Resonators for Wideband Filtering," *IEEE Trans. Microw. Theory Tech.*, vol. 61, no. 1, pp. 403–414, Jan. 2013.

[35] T. Manzaneque, R. Lu, Y. Yang, and S. Gong, "Lithium Niobate MEMS Chirp Compressors for Near Zero Power Wake-Up Radios," *J. Microelectromechanical Syst.*, vol. 26, no. 6, pp. 1204–1215, Dec. 2017.

[36] A. Demma, P. Cawley, and M. Lowe, "Scattering of the fundamental shear horizontal mode from steps and notches in plates," *J. Acoust. Soc. Am.*, vol. 113, no. 4, pp. 1880–1891, Apr. 2003.

[37] T. Kodama, H. Kawabata, Y. Yasuhara, and H. Sato, "Design of Low-Loss SAW Filters Employing Distributed Acoustic Reflection Transducers," in *IEEE 1986 Ultrasonics Symposium*, 1986, vol. 70, no. 9, pp. 59–64.

[38] C. S. Hartmann and B. P. Abbott, "Overview of design challenges for single phase unidirectional SAW filters," in *Proceedings., IEEE Ultrasonics Symposium*, 1989, pp. 79–89.

[39] S. Datta, *Surface acoustic wave devices*. Prentice-Hall, 1986.

[40] M. Koshiba, K. Hasegawa, and M. Suzuki, "Finite-Element Solution of Horizontally Polarized Shear Wave Scattering in an Elastic Plate," *IEEE Trans. Ultrason. Ferroelectr. Freq. Control*, vol. 34, no. 4, pp. 461–466, 1987.

[41] R. Lu, T. Manzaneque, Y. Yang, and S. Gong, "Lithium Niobate Phononic Crystals for Tailoring Performance of RF Laterally Vibrating Devices," *IEEE Trans. Ultrason. Ferroelectr. Freq. Control*, vol. 3010, no. c, pp. 1–1, 2018.

[42] S. Datta and B. J. Hunsinger, "An analytical theory for the scattering of surface acoustic waves by a single electrode in a periodic array on a piezoelectric substrate," *J. Appl. Phys.*, vol. 51, no. 9, pp. 4817–4823, Sep. 1980.

[43] Dong-Pei Chen and H. A. Haus, "Analysis of Metal-Strip SAW

Gratings and Transducers," *IEEE Trans. Sonics Ultrason.*, vol. 32, no. 3, pp. 395–408, May 1985.

[44] E. W. Weisstein, "Exponential Sum Formulas." [Online]. Available: http://mathworld.wolfram.com/ExponentialSumFormulas.html.

[45] W. R. Smith, H. M. Gerarl, and W. R. Jones, "Analysis and Design of Dispersive Interdigital Surface-Wave Transducers," *IEEE Trans. Microw. Theory Tech.*, vol. 20, no. 7, pp. 458–471, 1972.

[46] I. E. Kuznetsova, B. D. Zaitsev, S. G. Joshi, and I. A. Borodina, "Investigation of acoustic waves in thin plates of lithium niobate and lithium tantalate," *IEEE Trans. Ultrason. Ferroelectr. Freq. Control*, vol. 48, no. 1, pp. 322–328, Jan. 2001.

[47] Y. H. Song and S. Gong, "Elimination of spurious modes in SH0 Lithium Niobate laterally vibrating resonators," *IEEE Electron Devices Lett.*, vol. 36, no. 11, pp. 1198–1201, 2015.

[48] K. Y. Hashimoto, *Surface Acoustic Wave Devices in Telecommunications: Modelling and Simulation*. Springer Berlin Heidelberg, 2013.

Tomás Manzaneque (M'14) received the Ph.D. degree in industrial engineering from the University of Castilla-La Mancha, Spain, in 2015, with focus on applying piezoelectric MEMS resonators as sensors for measuring the density and viscosity of liquids. In the same year, he joined the Micro and Nanotechnology Laboratory, University of Illinois at Urbana–Champaign, USA, as a postdoctoral researcher. During this period he focused on acoustic devices for low power radio receivers in Internet of Things applications. In 2018, he moved to Delft University of Technology, The Netherlands, as a postdoctoral researcher, where he is currently working on microfluidic MEMS for biological applications. He has authored or co-authored more than 20 journal papers covering the design, modeling, characterization, and integration of piezoelectric micro-devices.

Ruochen Lu (S'14) received the B.E. degree with honors in microelectronics from Tsinghua University, Beijing, China, in 2014, and the M.S. degree in electrical engineering from the University of Illinois at Urbana– Champaign, Urbana, IL, USA, in 2017, where he is currently pursuing the Ph.D. His research interests include radio frequency microsystems and their applications for timing and signal processing. He received the Best Student Paper Awards at 2017 IEEE International Frequency Control Symposium, and 2018 IEEE International Ultrasonics Symposium. He is also a recipient of the 2015 Lam Graduate Award from the College of Engineering, UIUC, the 2016 Nick Holonyak, Jr. Graduate Research Award and the 2017 Nick Holonyak, Jr. Fellowship from the Department of Electrical and Computer Engineering at UIUC.
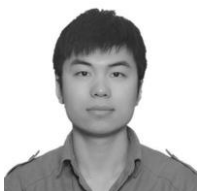
Yansong Yang (S'15) received the B.S. degree in electrical and electronic engineering from the Huazhong University of Science and Technology, Wuhan, China, in 2014, and the M.S. degree in electrical engineering from the University of Illinois at Urbana–Champaign, Urbana, IL, USA, in 2017, where he is currently pursuing a Ph.D. degree in Electrical Engineering. He has won the 2nd Place in Best Paper Competition at the 2018 International Microwave Symposium and has been a finalist for the Best Paper Award at 2018 IEEE International Frequency Control Symposium. His research interests include design and microfabrication techniques of MEMS resonators, filters, and switches for RF front-ends and wake-up systems.
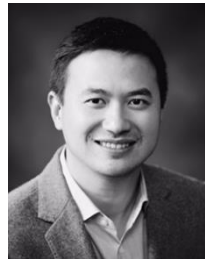
Songbin Gong (S'06–A'09–M'12–SM'17) received the Ph.D. degree in electrical engineering from the University of Virginia, Charlottesville, VA, USA, in 2010. He is currently an Assistant Professor and the Intel Alumni Fellow with the Department of Electrical and Computer Engineering and the Micro and Nanotechnology Laboratory, University of Illinois at Urbana–Champaign, Urbana, IL, USA. His research primarily focuses on design and implementation of radio frequency microsystems, components, and subsystems for reconfigurable RF front ends. In addition, his research explores hybrid microsystems based on the integration of MEMS devices with photonics or circuits for signal processing and sensing. He is a recipient of the 2014 Defense Advanced Research Projects Agency Young Faculty Award and the 2017 NASA Early Career Faculty Award. Along with his students and postdocs, he received the Best Paper Award from the 2017 IEEE International Frequency Control Symposium, the 2018 International Ultrasonics Symposium, and won 2nd place in Best Paper Competition at the 2018 IEEE International Microwave Symposium. He has been a guest editor for the special issue on RF-MEMS in the Journal of Micromechanics and Microengineering, and also a Technical Committee Member of MTT-21 RF-MEMS of the IEEE Microwave Theory and Techniques Society, International Frequency Control Symposium, and International Electron Devices Meeting.